Space Rendezvous Laboratory
Department of Aeronautics and Astronautics
Stanford University
https://slab.stanford.edu/

Development and Verification of the Stanford GNSS Navigation Testbed for Spacecraft Formation Flying

Vince Giralo, Duncan Eddy, and Simone D'Amico

Jul. 18, 2017

Technical Report No: TN2017-001

Contents

Abstract

Distributed space missions promise advances in space science, planetary science, and on-orbit servicing. Many of these concepts rely on centimeter-level or better relative navigation solutions obtained through Global Navigation Satellite Systems (GNSS) based guidance, navigation and control functionalities on cooperative satellites. The development of these GNSS technologies to meet next-generation mission requirements necessitates a high-fidelity testing environment. This research presents the design, development, and verification of the Stanford GNSS testbed for spacecraft formation flying. A detailed explanation of the system architecture, hardware components, and simulation software is given. Furthermore, this work introduces a cross-verification method for the GNSS hardware-in-the-loop testbed itself. An extended Kalman filter is used to quantify the distribution of pseudorange and carrier-phase measurement residuals from a live-signal source. The measurement residual statistics, along with satellite tracking-performance, are used as a comparison metric to verify that all stimulation methods are consistent with live-signals. A characterization of a GNSS receiver is conducted using a zero-baseline test after verification. The calibrated system is used to assess the performance of prototype algorithms for precise absolute and relative navigation of small-satellite space systems, specifically nanosatellites such as CubeSats.

1 Introduction

Distributed satellite systems use multiple spacecraft working together in a coordinated manner to accomplish a mission objective that would be challenging, if not impossible, to achieve with a single large spacecraft. Applications of distributed space systems include close-proximity operations such as on-orbit servicing and assembly[1] as well as science applications like exo-planet imaging[2] or synthetic aperture radar interferometry[3]. The exploitation of scientific measurements require knowledge of the absolute orbit of a spacecraft, and the relative orbit with respect to another cooperating spacecraft. Global Positioning System (GPS) receivers are recognized as the best device for providing onboard navigation wherever GPS signals are present. PRISMA[4] and TanDEM-X[5] are examples of successful autonomous formation flying missions in low Earth orbit (LEO) where GPS is the primary method for orbit determination. As missions become increasingly reliant on GPS for navigation, realistic Hardware-In-the-Loop (HIL) testing of Guidance, Navigation, and Control (GNC) functionalities based on GPS receivers is critical to ensure the success of the mission.

As micro- and nano-satellites transition from being merely an educational tool to a viable scientific platform, many small satellite-based distributed mission concepts have been proposed[6]. Due to the power, volume, mass, and cost constraints of small satellite systems, space-hardened receivers like the BlackJack [7] are not feasible options for onboard navigation, therefore Commercial-Off-The-Shelf (COTS) receivers are used in their stead. While COTS receivers provide many advantages over mission-specific devices, such as an increased number of channels, low power-consumption, and small volume and mass, there has not been a rigorous assessment of their viability for precise orbit determination and onboard navigation. This is a necessary step in assessing the feasibility of new small satellite mission concepts.

Additionally, as new Global Navigation Satellite System (GNSS) constellations beyond GPS and GLONASS become operational (e.g. Galileo, Beidou), the addition of new signals and frequencies presents the possibility to provide improvements in integer ambiguity resolution and signal availability for above-the-constellation navigation.[8] Given the work-in-progress status of these constellations, the full potential can currently only be assessed in simulation.

A realistic HIL testbed enables stimulation of GNSS-based onboard navigation systems in a manner consistent with the flight environment. This is required for a critical assessment of the system performance since orbital scenarios present a uniquely challenging set of operational conditions for GNSS receivers that cannot be replicated on ground. Spaceborne GNSS receivers have to cope with large Doppler shifts, phase wind-up of the carrier signal, short tracking arcs, and rapidly varying constellation geometries. If the receiver firmware and the navigation algorithms are not properly adjusted to account for these conditions the navigation performance could be severely degraded or the receiver might not be able to achieve a tracking lock at all. By interfacing high-fidelity orbit propagation software with a GNSS signal simulator, it becomes possible to stimulate a receiver with Radio Frequency (RF) signals representative of what would be seen on orbit.

The first closed-loop HIL testbed for GPS-based formation flying, known as the Formation Flying Test Bed (FFTB), was created by Leitner[9] at Goddard Space Flight Center (GSFC). This testbed is capable of simulating GPS L1 and L2 frequencies for each of up to four spacecraft. The FFTB testbed has been used by Burns et al.[10] to demonstrate formation control, by Gill et al.[11] to simulate autonomous formation flying, and by Winternitz[12] to validate the above-the-constellation GPS navigation system of the Magnetospheric Multi-Scale (MMS) mission. The German Space

Operations Center developed a GPS-based HIL testbed that has been used extensively in the development of autonomous formation flying capabilities. Leung[13] used the testbed to demonstrate relative navigation of a four-satellite formation, while D'Amico et al.[14, 15] used it extensively for the development of the PRISMA autonomous navigation system. Other GPS testbeds include those of Kowalchuck[16] and Park et al.[17] which were developed to aid in formation flying GNC research. More recently, Montenbruck et al.[18] and Biswas et al.[19] have used testbeds that are capable of simulating constellations other than GPS, specifically GLONASS and Galileo, to investigate single-satellite navigation algorithms.

This work presents the design, development, and use of the Stanford GNSS Navigation Testbed (SGNT) for hardware-in-the-loop testing of GNSS receivers and satellite navigation systems. The HIL testing system provides multiple methods for characterizing and testing GNSS receivers and related GNC algorithms. Multiple testing modes, each of increasing simulation complexity and fidelity, are available. In the most basic configuration, a software receiver emulator is used to generate sets of GNSS measurements in faster-than-real-time allowing for rapid evaluation and iteration of navigation algorithms in different operational scenarios. More realistic testbed configurations seamlessly exchange the receiver emulator for a live RF signal from either a rooftop antenna or a GNSS Signal Simulator (GSS). The antenna allows for testing with true GNSS signals from multiple constellations and frequencies, while the GSS allows for a user-defined environment with multiple RF outputs, allowing for flexibility in scenario definitions. The ability to reproduce a scenario observed by a static antenna with the receiver software emulator and the GSS provides a cross-validation baseline for each simulation method to ensure the fidelity and consistency between methods. The support of static test scenarios also enables GNSS receiver noise characterization through zero-baseline testing. In the most complex operational mode, orbits of multiple cooperating satellites are simulated in real-time and used by the GSS to generate representative RF signals for each trajectory.

One project the Stanford GNSS Navigation Testbed is currently supporting is the Distributed Timing and Localization (DiGiTaL) system. DiGiTaL is a NASA Small Spacecraft Technology Program (SSTP) development project, creating a 0.5U form-factor payload that provides centimeter-level navigation accuracy in real-time and nanosecond-level time synchronization for formations of any number of satellites. This is accomplished through the integration of a COTS GNSS receiver, a Chip-Scale Atomic Clock (CSAC), and a dedicated Inter-Satellite Link (ISL) into a single unit. The ISL allows for sharing of carrier-phase observations among cooperating satellites, which enables the use of low-noise single-difference carrier-phase measurements for precision estimation of the relative formation state. Through rigorous testing of two engineering units in both the SGNT and FFTB at Stanford and GSFC, respectively, DiGiTaL will raise the technology readiness level (TRL) of precision navigation for small satellite formations from 3 to 6. In this paper, the HIL testing system at Stanford is used to validate prototype algorithms for the DiGiTaL satellite navigation system. Key results from the tests of prototype algorithms for absolute and relative navigation accuracy are presented and discussed.

This general introduction is followed by a description of the testbed architecture and each constituent component. The third section focuses on how a static test scenario can be implemented using the testbed for cross-comparison and GNSS receiver characterization. The fourth section describes the orbit propagation software responsible for dynamic simulation capabilities and presents key comparisons against mission data. The fifth section presents formation flying navigation re-

sults from prototype DiGiTaL navigation algorithms. The sixth and final section addresses lessons learned, the way forward, and concluding remarks.

2 System Architecture and Development

In this section, the modular design, development process, and operational configurations of the testbed are discussed. Any HIL testbed can be conceptually divided into two functional partitions—the environmental simulation and the test article. Figure 1 depicts this conceptual design of the HIL testbed. The environmental simulation is responsible for modeling the true system state and generating measurements either through a software measurement model or RF stimulation (cf. Figure 1 left block). The test article can be anything from GNC algorithms processing recorded measurements post-facto to a complete, integrated GNC system. Such a system would be comprised of a GNSS receiver with a on-board computer processing measurements (pseudorange, carrier-phase, Doppler shift, and broadcast ephemeris) and applying algorithms for estimation and control in real-time (cf. Figure 1 right block). At this point, it should be noted that no assumptions have been made regarding the dynamics of the environmental simulation. The complexity of this simulation is up to the user, and allows for high-fidelity truth scenarios while using reduced-dynamics for the GNC algorithms to reduce computational load.

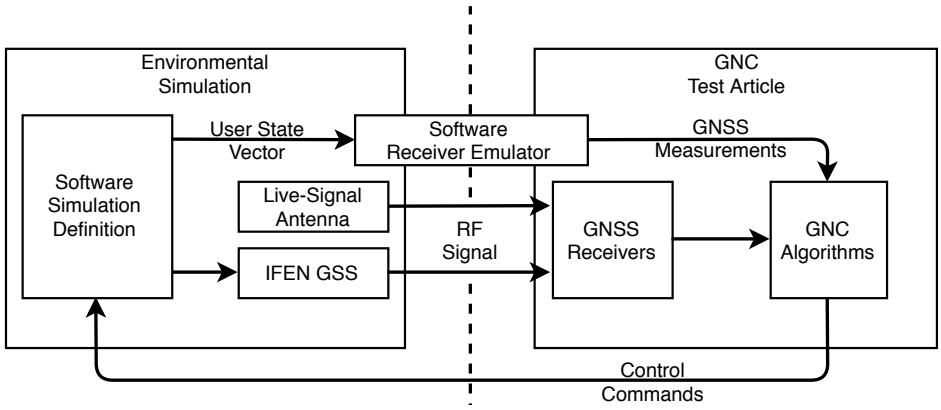

Figure 1: Overview of SGNT conceptual design and information flow in the system.

Approaching the creation of the testbed with this design concept in mind enables its development to proceed in a sequential manner—beginning with the implementation of basic, software-only capabilities then methodically adding new functionality, either in the environmental simulation or the test-article, until full closed-loop validation of a satellite GNC hardware/software system is possible.

2.1 Dynamics Simulation

The backbone of the HIL environmental simulation is the real-time orbit propagation software. For the testbed to act in support of precision GNC for space missions, where position errors at the centimeter-level are significant, it is essential that the simulation be able to reproduce the true orbital dynamics to the utmost level of fidelity possible. Fundamentally, the dynamic model used in the simulation determines the performance of any subsequent estimation or control algorithms. The dynamics used for navigation are low-fidelity, and the closer these dynamics are to the true dynamics, the better the navigation solution will be. Therefore, rigorous performance

characterization necessitates modeling orbit and attitude dynamics that are consistent with the required navigation accuracy.

Furthermore, the satellite trajectory—both the orbit and inertial attitude—directly determines the operational environment of a GNSS receiver as well as any associated challenges. While receivers on-ground see Doppler shifts no larger than 5000 Hz, a receiver in Low Earth Orbit (LEO) can experience Doppler shifts as large as 45,000 Hz. Receivers operating in LEO are further subject to short tracking arcs, where a single GNSS satellite remains visible for no longer than 15 minutes on average. When attempting precision navigation using differential GNSS, the number of commonly visible satellites is also an essential operational constraint that must be captured in simulation.

The simulation software must include both high fidelity orbital and attitude dynamics models, and they must be able to run in real-time for multiple satellites with time-synchronization across all spacecrafts. To meet these needs, the Space Rendezvous Laboratory (SLAB) has developed the SLAB Satellite Software ($\mathcal{S}^3$) toolkit. Its design, capabilities, and validation against PRISMA mission flight products are presented and discussed in the fourth section of this paper.

2.2 Software Receiver Emulator

The next step in constructing the testbed was to develop a software emulator of a GNSS receiver. Numerical propagation of the equations of motion coupled with the receiver emulator provides the minimum necessary functionality for GNSS-based GNC algorithm testing. The receiver emulator takes as inputs the user state vector (from the dynamics simulation), the state vectors of the GNSS constellation satellites (from either IGS Final Products[20] or RINEX ephemerides), and the current simulation time. All state vectors are provided in the Earth-Centered, Earth-Fixed (ECEF) frame, and all times are provided in GPS time, regardless of the actual constellation used. The emulator generates as outputs the pseudorange, carrier-phase, and Doppler shift measurements corrupted by receiver-specific noise for each GNSS constellation and frequency. A receiver emulator has the added benefit of being able to generate measurements in faster-than-real-time, allowing for quick software-only testing and iteration of algorithms. The emulator uses a standard model of GNSS pseudorange, ρ_{pr}, and carrier-phase, ρ_{cp}, at time t, given by

$$\begin{aligned} \rho_{pr}(t) &= ||\mathbf{r}(t) - \mathbf{r}_{GNSS}(t-\tau)|| + c(\delta t - \delta t_{GNSS}) + I + T + \epsilon_{pr} \\ \rho_{cp}(t) = \lambda\Phi &= ||\mathbf{r}(t) - \mathbf{r}_{GNSS}(t-\tau)|| + c(\delta t - \delta t_{GNSS}) - I + T + \lambda N + \epsilon_{cp} \end{aligned} \tag{1}$$

In this model, $\mathbf{r}$ is the position vector of the user's antenna and $\mathbf{r}_{GNSS}$ is the position vector of the GNSS satellite's antenna. The clock offset of both the receiver and the GNSS system are given by δt and δt_{GNSS}, respectively. This model includes the effects of signal time-of-flight, τ, Ionospheric path delay, I, Tropospheric path delay, T, and the added uncertainty of integer ambiguities, N, which is multiplied by the wavelength of the incoming signal, λ. These values are dependent on the scenario definition, and independent of the hardware used. However, the receiver-specific noise values, ϵ_{pr} and ϵ_{cp}, remain uncertain quantities. Every physical GNSS receiver is subject to measurement errors due to thermal noise in the electronics, signal tracking errors introduced by the delay- and phase-lock-loop settings, and manufacturing variations. These noise values vary not just

between receiver models, but also between individual units. They are impossible to know a-priori and can only be quantified through hardware characterization. To develop a rigorous simulation of all components, the hardware receiver being emulated in software must be incorporated into the testbed and stimulated with RF signals, either by an antenna or by a GSS. This allows for a zero-baseline test to be conducted to deduce the receiver-specific noise. This test is discussed in the third section of this paper.

2.3 IFEN GNSS Signal Simulator

The central component of the testbed that enables replacing the receiver software emulator with a hardware receiver for hardware-in-the-loop capabilities is an IFEN NavX Professional[21] multi-GNSS signal simulator, shown in Figure 2. The NavX Professional is capable of simulating 72 independent signals, divided between two independent RF outputs. The unit is currently able to simulate GPS L1, Galileo E1, Beidou B1, QZSS, and IRNSS signals. Its capabilities can be further extended through a software license upgrade to include the L2, L5, E5a, E5b, E6, B2, and B3 signals.

Figure 2: IFEN multi-GNSS signal simulator (top) pictured along with a Septentrio AsteRx4 receiver OEM development board (bottom).

The IFEN GSS extends the capabilities of the testbed, but a verification step must first be done to show that it can produce RF signals that are representative of the signals from the true GNSS constellations. Therefore, it is necessary to introduce a means to cross-check the behavior of the GSS. This check was accomplished by adding a static ground-antenna to the HIL testbed. The selection of the antenna and the cross-comparison between stimulation methods is discussed in the next section.

2.4 DiGiTaL Test Article

Once the testbed has been developed, a test article can be assessed and used for HIL development and deployment of algorithms. In the most general terms, a test article is comprised of three components: a GNSS receiver for processing RF signals and extracting navigation measurements, an ISL for sharing GNSS measurements between cooperative satellites, and a flight computer to both process measurements (from either the receiver or ISL) and execute GNC programs. The DiGiTaL system, represents an ideal example of such a test article. Figure 3 shows two prototype DiGiTaL units in a break-out form.

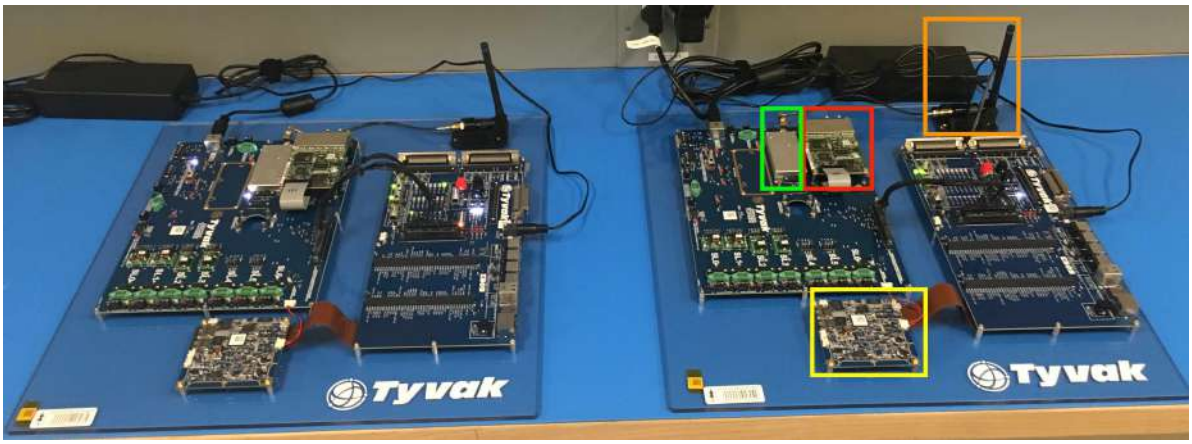

Figure 3: Two prototype DiGiTaL units. Components include: flight computer (yellow), Novatel OEM628 GNSS receiver (red), UHF radio (green), inter-satellite link antenna (orange).

Table 1 provides the specifications of the constituent components of the DiGiTaL system. Two test systems were acquired from Tyvak NanoSatellite Systems as pre-integrated units broken out in flat-sat form for ease of use.

On-Board Processors		Radio ISL	
Command & Data Handling Processor		Frequencies	400-470 MHz
Architecture	ARM9		800-930 MHz
Clock Speed	400 MHz	Data Rates	1.2 - 250 kbps
Power Consumption	$<$ 0.200 W	*Power Consumption*	
GNC Application Processor		RF TX	Up to 2 W
Architecture	ARM Cortex A8+	DC TX	7W
Clock Speed	800 MHz	DC RX	0.130 W
Mass	610 g	Mass 20 g	
Volume	83 x 83 x 53 mm	Volume	32 x 87 x 8mm
Power Consumption	$<$ 1 W	Power Consumption	$<$ 1.3 W

Table 1: Specification of DiGiTal System Components

Before selecting the GNSS receiver to use with the DiGiTaL system, a survey of COTS GNSS receivers suitable for use on small satellites was done. The criterion were a small board footprint ($\leq (100\ mm) \times (100\ mm)$) and low power consumption ($\leq 3\ W$). It was also necessary that the

chosen receiver was compatible with all current and planned GNSS constellations and frequencies, and with an external frequency reference. Preference was also given to receivers that had direct flight-heritage or so-called partial-flight heritage, defined by a receiver in the same family with flight heritage. From this survey, two receivers were determined to be best suited for precision navigation applications on small satellites—the Septentrio AsteRx4 and Novatel OEM628. While the Novatel was ultimately selected for use in the DiGiTaL prototype, a Septentrio AsteRx4 was also acquired by SLAB for comparison.

2.5 Implementation of Open and Closed-Loop HIL Testing

The testbed components were assembled into working open-loop and closed-loop simulation configurations. An open-loop configuration is defined as having no orbit or attitude maneuvers computed by the spacecraft GNC system in real-time as a function of the state. Therefore, the complete orbital trajectory is defined by the initial conditions and can be precomputed. This does not allow for validation of a full GNC system—in-particular, the guidance and control portions. However, the closed-loop configuration allows for maneuvers to be computed in real-time and fed back into the propagation to test the guidance and control algorithms. Figure 4 depicts a closed-loop configuration for final validation of the DiGiTaL system.

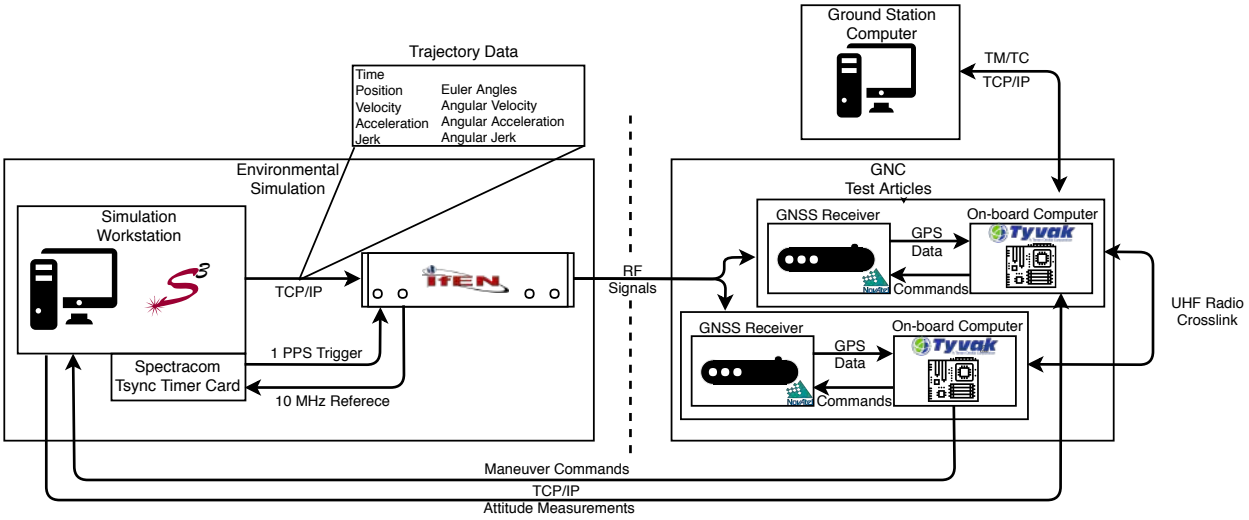

Figure 4: Schematic of the closed-loop HIL testbed configured for DiGiTaL testing.

For the most general simulations, the orbital trajectory must be recomputed in response to the execution of maneuvers or attitude actuations. Maneuvers performed by the test article in response to navigation data are reflected first in the simulation trajectory then subsequently in the IFEN GSS RF output, the receiver measurements, and finally in the navigation algorithms output. This integrated test configuration is referred to as closed-loop and is able to assess the strongly coupled behavior of navigation and orbit control systems.

In order to realize either open- or closed-loop testing capabilities, a number of further additions to the testbed had to be made. First, a custom-built workstation (cf. Figure 4 left), optimized for single-thread computational performance is used to host all environmental simulation as well as to

configure the test settings. The host workstation also serves to host any receiver emulators as well as monitor the simulation status. A second computer (cf. Figure 4 upper right) is also introduced to mimic ground-station functionality—sending telecommands to the test article over TCP/IP and downlinking any telementry.

It is also essential to synchronize the dynamics simulation to be in lock-step with the GNSS signal simulator. This synchronization is accomplished through the addition of a Spectracom TSync Timing Card[22] to the workstation. The timing card can transmit and receive 1PPS 3V TTL or 10 MHz reference signals and use these signals to condition the simulation clock to be in sync with the GSS. If a timing card were not included, a drift between the two device clocks would occur. The trajectory data exchanged between the software simulation and the GSS would become inconsistent over time, causing invalid measurements to be created. This delay and resulting inconsistency are not acceptable for rigorous validation of GNC flight software.

At this point, the SGNT outline has been presented. The constituent components of the testbed have been introduced, as well as the motivation for their inclusion. The sections that follow cover the static testing applications of the SGNT, a detailed discussion of the high-fidelity dynamics simulation of orbital trajectories, and the results of an SGNT open-loop test of DiGiTaL navigation algorithms.

3 Static Testing For Receiver Characterization

In this section, the implementation of static testing procedures supported by the testbed and their use are explained. While the primary purpose of the testbed is to support orbital navigation system testing, the addition of static testing capabilities serves two purposes. The first is to provide a check on the receiver emulator and GSS components of the testbed, ensuring they are properly functioning and calibrated. The second is to provide a means of receiver noise characterization through zero-baseline testing. The ability to accurately assess receiver noise properties allows for improved receiver emulator models and navigation filter tuning.

To ensure that the GNSS receiver emulator is an accurate model of a true GNSS receiver, a comparison between the outputs of the emulator and those of a live antenna with an attached receiver was performed. A Septentrio PolaNt Choke Ring B3/E6 antenna was placed on the roof of the William F. Durand building at Stanford University, and connected to the Septentrio AsteRx4 GNSS receiver. This antenna was chosen due to the choke ring feature, which provides improved multi-path rejection and low phase-center variation compared to a traditional patch antenna. This antenna is also compatible with the full range of GNSS signal bands and can be seen mounted on the roof in Figure 5. In addition to validating the receiver emulator against the live data, the consistency of GSS-based simulations can also be assessed by attempting to reproduce the static-antenna test results after the fact.

Figure 5: Septentrio Choke Ring antenna mounted at Stanford University

3.1 Test Setup

To begin the cross-comparison, the live antenna and receiver were used to collect what is considered the truth observables for the test. This data contains broadcast ephemerides and an observation file with pseudorange, carrier-phase, doppler measurements, and carrier-to-noise ratios (C/N_0). To extract a precise position from this data, the observation file was processed using the Natural Resources Canada's (NRC) fast precise-point positioning (PPP) service[23, 24]. This is a user-friendly service provided by the Canadian government for a variety of applications, including surveying, mapping, and navigation. Precise orbit products for the GNSS satellites are used in conjunction with the measurements in the observation file to create a baseline position estimate accurate to the centimeter-level.

Comparison tests were then set up by recreating this static scenario using both the receiver emulator and GSS for environmental simulation. To accurately match the test conditions, the state of the GNSS constellations had to be carefully reproduced. Precise orbit products were retrieved from the International GNSS Service (IGS), which provide the GNSS satellite locations currently accurate to 2.5 cm for GPS and 20 cm for Beidou and Galileo. The testbed scenario also includes the Ionospheric path delay, as modeled using Klobuchar constants from the broadcast ephemeris information, and Tropospheric path delay, as well as a model of the antenna gain pattern. Table 2 describes the scenario parameters that were used for both the receiver emulator and the GSS tests.

Parameter	Value
Initial Epoch	April 21, 2017, 00:00:00 GPST
Final Epoch	April 22, 2017, 00:00:00 GPST
Latitude	37° 25' 36.9852"
Longitude	-122° 10' 23.7379"
Altitude	19.899 m
GNSS Systems	GPS, GAL, BDS

Table 2: Static Test Configuration Settings

3.2 Test Results

Tests were conducted to compare the rooftop live antenna, software receiver emulator, and the GSS, and the validity of each signal generation method was analyzed. The live antenna test was used as a reference because no simulation is done in this case, and all the information is coming from the true GNSS satellites. The receiver emulator and GSS tests were then compared against the live antenna test, and three metrics were used: satellite tracking, signal C/N_0, and the navigation solution. Satellite tracking was analyzed by use of a skyplot, which shows the trajectories of each GNSS satellite as a function of the azimuth and elevation with respect to the antenna's ground plane. The skyplots from each test are shown in Figure 6.

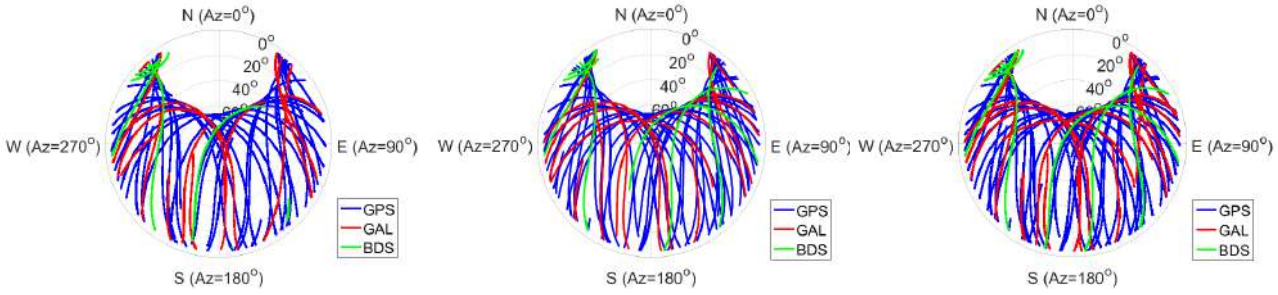

Figure 6: Tracked satellite trajectories with respect to the antenna plane from rooftop live antenna (left), receiver emulator test (center), and GSS test (right)

Compared to the live test, the receiver emulator and GSS tests show 2 more BeiDou satellites and 4 more Galileo satellites being tracked, particularly for lower elevations. The emulator and GSS tests show nearly identical satellite tracking. This suggests that either there are line-of sight obstructions preventing the live antenna from receiving low-elevation signals, or both the receiver emulator and

GSS are neglecting low elevation signal-propagation effects. However, the vast majority of tracked satellites is the same between tests, providing a first positive confirmation of each testing method.

The second simulation-consistency metric is the signals' carrier-to-noise ratios. Figure 7 shows the C/N_0 as measured by the receiver in each case. As expected, there is a decrease in C/N_0 with decreasing elevation, which is a result of decreased antenna gain at low elevations. Differences between the three tests occur near the lowest elevations, specifically less than 20 degrees. In the live test, there is a variation in noise of 15 dB-Hz at these elevations, compared with 5 dB-Hz in the receiver emulator and GSS tests. This is attributed to unmodeled multi-path effects. Although the antenna was selected such to mitigate these effects, it cannot completely remove them. Since these effects were assumed to be small, the simulation scenarios were defined without multi-path. This indicates that for orbital scenarios where multi-path effects may be present (possibly due to deployable solar panels), it will be necessary to include multi-path effects in simulation due to their effect on measurement noise.

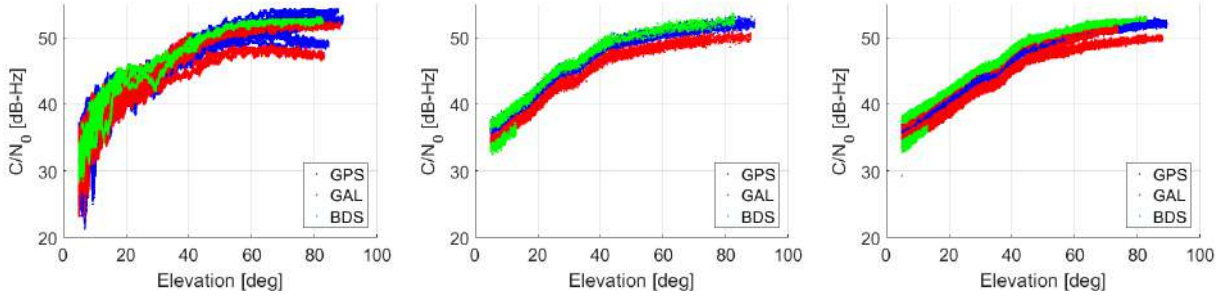

Figure 7: Signal carrier-to-noise ratio from rooftop live antenna (left), receiver emulator test (center), and GSS test (right)

The final cross-comparison between live-antenna, receiver emulator, and GSS stimulation methods was done by evaluating the accuracy of the navigation solution from each test. To this end, an extended Kalman filter (EKF) was developed and used with each test, taking as inputs the raw measurements (pseudorange and carrier-phase), and outputting a static position estimate. The following describes the development of the EKF used in the analysis. This approach presented here will be further built upon for use in orbital scenarios, and therefore is a key step.

The pseudorange and carrier-phase measurement model is presented in Equation 1. To eliminate Ionospheric delays, the Group and Phase Ionospheric Calibration[25] (GRAPHIC) measurements were formed from the combination of the code and phase measurements, as given by

$$\rho_{gr} = \frac{\rho_{pr} + \rho_{cp}}{2} = ||\mathbf{r}(t) - \mathbf{r}_{GNSS}(t-\tau)|| + c(\delta t - \delta t_{GNSS}) + T + \lambda\frac{N}{2} + \epsilon_{gr} \tag{2}$$

where $\epsilon_{gr} \approx \epsilon_{pr}/2$. Although the ionospheric delay has been eliminated, the tropospheric delay term is still present and must therefore be modeled. This is accomplished with the Minimum Operational Performance Standards [26] (MOPS) model, which divides the delay into dry hydrostatic and wet-zenith delay components. These are then mapped to different elevations using the Neill mapping function [27]. This model is given by

$$T = T_{z,dry} M_{dry} + T_{z,wet} M_{wet} \tag{3}$$

where T is the total tropospheric delay, T_z is the zenith tropospheric delays, M represents the mapping functions. To account for variations in the wet delay component, which varies based on local weather conditions, the zenith wet delay is augmented with a correction factor, ΔT, modeled as a random walk process, given by

$$T_{z,wet} = T_{z0,wet} + \Delta T_{z,wet} \tag{4}$$

At this point, the full estimation state can be written as

$$\mathbf{x} = [\mathbf{r} \;\; \mathbf{c\delta t} \;\; \mathbf{N} \;\; \Delta T_{z,wet}]^T \tag{5}$$

where $\mathbf{r}$ is the Earth-Centered, Earth-Fixed Cartesian coordinates of the antenna phase center, $\mathbf{c\delta t}$ is the vector of receiver clock offsets with respect to each GNSS constellation time, N is the vector of real-valued carrier-phase biases for each tracked signal, and $\Delta T_{z,wet}$ is the tropospheric adjustment. For a filter using GPS (30 satellites), Galileo (14 satellites), and BeiDou (13 satellites), this becomes a 64-dimensional state.

Since the antenna position is known to be fixed, and all other state variables are modeled as random-walk processes or constants, the state transition matrix $\mathbf{\Phi}_{t,t_0}$ for the time-update simplifies to the identity matrix

$$\mathbf{\Phi}_{t,t_0} = \frac{\partial \mathbf{x}_t}{\partial \mathbf{x}_{t_0}} = \mathbf{I}_{64\times 64} \tag{6}$$

where $\mathbf{x}_t$ and $\mathbf{x}_{t_0}$ describe the state at time t and t_0 respectively, and $\mathbf{I}$ is a 64×64 identity matrix.

The variance of the variables modeled as random walks is described by

$$q_i = \frac{\sigma_i^2 \, (t - t_0)}{\tau_i} \tag{7}$$

which is added as process noise to the filter. The subscript i represents the given variable (either the clock offset, $\mathbf{c\delta t}$, or the tropospheric correction, $\Delta T_{z,wet}$), and τ is the process-specific auto-correlation time constant.

For the measurement update phase of the EKF, the measurement sensitivity matrix, $\mathbf{H}$, describes the expected change in measurement due to a change in state. It is calculated as the partial derivatives of the measurement model with respect to the state. For GRAPHIC measurements the sensitivity matrix is given by

$$\mathbf{H}_t = \frac{\partial \mathbf{z}_t}{\partial \mathbf{x}_t} = [-\mathbf{e} \;\; \mathbf{1} \;\; \lambda/\mathbf{2} \;\; M_{wet}]_{1\times 64} \tag{8}$$

where $\mathbf{z}$ is the modeled measurement. The partial with respect to the clock offset takes a value of 1, and with respect to the carrier-phase bias is half the wavelength, $\lambda/2$. The partial of the measurements with respect to the range is given as the negative of the line-of-sight vector from the satellite to the receiver [28]. The first order approximation of this vector is given by

$$\frac{\partial \mathbf{z}_t}{\partial \mathbf{r}_t} = -\mathbf{e} = -\frac{\mathbf{r}_{GNSS} - \mathbf{r}}{||\mathbf{r}_{GNSS} - \mathbf{r}||} \tag{9}$$

The input parameters for the EKF are shown in Table 3 and were the same for all conducted tests.

Parameter	Value	Parameter	Value
A-priori standard deviation		*Process noise*	
σ_r [m]	10.0	$\sigma_{c\delta t}$ [m]	1.0
$\sigma_{c\delta t}$ [m]	10.0	$\sigma_{\Delta T_{z,wet}}$ [m]	0.1
σ_N [cycles]	5.0		
$\sigma_{\Delta T_{z,wet}}$ [m]	0.1	*Measurement standard deviation*	
		σ_{gr} [m]	0.5
Auto-correlation time scale			
$\tau_{c\delta t}$ [s]	100.0		
$\tau_{\Delta T_{z,wet}}$ [s]	1000.0		

Table 3: Extended Kalman filter Parameters.

This method of estimation was used to determine the state of the system. The ECEF position estimates from each test are shown in Figure 8. Here, the ground truth position is subtracted from the state estimate to form the error. Comparing the solution from the live-antenna data, the receiver emulator test, and the GSS test, the maximum mean error in one direction is 0.48 m. This value is on the order of the broadcast ephemeris error, and therefore can be seen as the lower bound on navigation accuracy when the broadcast ephemerides are used to provide GNSS constellation information instead of IGS products. The error-bounds for each test are also consistent, with corresponding directions showing a maximum of 7 mm difference between any two tests. Each test shows maximum variance in the y-component, and minimum variance in the x-direction.

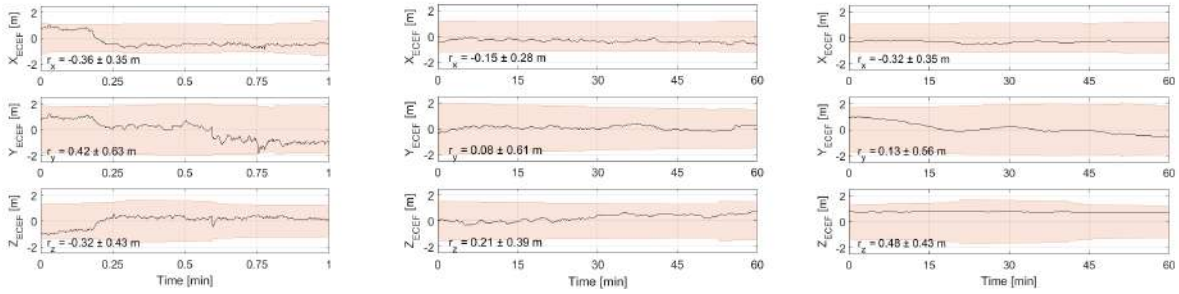

Figure 8: Position errors with 3σ bounds for a 1-hour arc from rooftop live antenna (left), receiver emulator test (center), and GSS test (right).

The filter output can also be compared in terms of post-fit residuals. The residuals for each test, shown in Figure 9, display a consistent band of white noise with standard deviations of

approximately 12 cm. There are a few instances of higher residuals, which occur when a new satellite enters into view. This causes the filter to initialize and estimate a new carrier-phase bias. The standard deviation on the residuals are representative of the noise of the AsteRx4 receiver for GRAPHIC measurements. This is shown in the next section, where the method for quantifying the level of noise is presented.

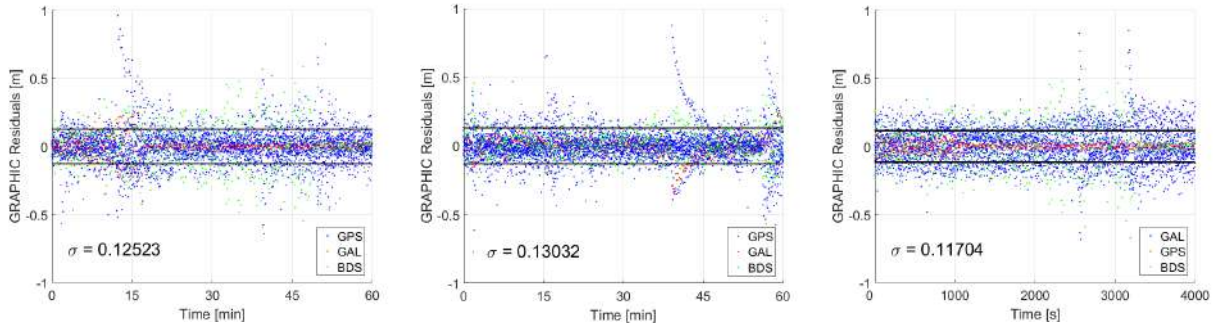

Figure 9: GRAPHIC measurement post-fit residuals from rooftop live antenna (left), receiver emulator test (center), and GSS test (right).

3.3 COTS Receiver Characterization

On-board GNSS-based satellite navigation systems have been able to achieve meter- and centimeter-level precision in absolute and relative positioning, respectively, in real-time. The ultimate lower-bound for real-time GNSS navigation accuracy, however, is determined by the noise of the used receiver. This drives the need to characterize the receiver to quantify the noise levels, which are required inputs to any EKF.

The quantification of receiver noise is accomplished through a process known as zero-baseline testing [29]. To perform this test, a receiver must be stimulated with two exact reproductions of the same scenario. While this is impossible to do for an individual unit using live signals[1], it can accomplished using a GNSS signal simulator. It was previously shown that the GSS in SLAB's testbed can be reliably used to replicate a live antenna scenario, and is therefore appropriate for use in a zero-baseline test. The presented work shows the characterization of the Septentrio AsteRx4, but can be identically repeated for any GNSS receiver.

To start, two identical scenarios must be run consecutively. The scenarios are configured to be error-free so to eliminate any chance for unwanted deviations between the two tests. This entails removing atmospheric delays and broadcast ephemeris errors. The simulated antenna location was placed in Hong Kong to maximize the number of BeiDou geostationary satellites that were in view.

The measurements from the two tests are combined to form double-differenced combinations. This is accomplished by first creating single-differenced values, given for pseudorange measurements by

[1] Typically a live signal is simultaneously fed to two identical receiver units, characterizing the noise of that receiver model.

$$\begin{aligned}\rho_{sdpr}^{(k)} &= \rho_{pr,u}^{(k)} - \rho_{pr,w}^{(k)} \\ &= \left(||\mathbf{r_u^{(k)}} - \mathbf{r_{GNSS}^{(k)}}|| + c(\delta t_u - \delta t_{GNSS}^{(k)}) + I_u^{(k)} + T_u^{(k)} + \epsilon_{pr,u}^{(k)}\right) \\ &- \left(||\mathbf{r_w^{(k)}} - \mathbf{r_{GNSS}^{(k)}}|| + c(\delta t_w - \delta t_{GNSS}^{(k)}) + I_w^{(k)} + T_w^{(k)} + \epsilon_{pr,w}^{(k)}\right) \\ &= \left(||\mathbf{r_{uw}^{(k)}} - \mathbf{r_{GNSS}^{(k)}}|| + c\delta t_{uw} + I_{uw}^{(k)} + T_{uw}^{(k)} + \epsilon_{pr,uw}^{(k)}\right)\end{aligned} \tag{10}$$

The superscript k denotes measurements coming from GNSS satellite k, and the subscripts u and w represent measurements being taken by receivers u and w, respectively. Forming the single difference eliminates any terms that only depend on the observed GNSS satellite, which in this case is the clock offset of that satellite and broadcast ephemeris errors.

By collocating the receivers in each test, any terms that depend on geometric conditions cancel out. This includes the range from the receiver to the transmitting satellite and atmospheric effects, although the latter were not included in the simulation. The reduced single-difference pseudorange equation is given by

$$\rho_{sdpr}^{(k)} = c\delta t_{uw} + \epsilon_{pr,uw}^{(k)} \tag{11}$$

A similar equation can be expressed for carrier-phase measurements, with the only difference being the inclusion of the carrier-phase bias. It is important to note this bias is independent for each received signal.

$$\rho_{sdcp}^{(k)} = c\delta t_{uw} + \lambda N_{uw}^{(k)} + \epsilon_{cp,uw}^{(k)} \tag{12}$$

These single-difference combinations for satellites k and l are then differenced to form the double-differenced observations. This combination eliminates all terms from the incoming signals with the exception of the noise, which is a product of the receiver. The resulting double-difference is given by

$$\begin{aligned}\rho_{ddpr}^{(k,l)} &= \rho_{sdpr}^{(k)} - \rho_{sdpr}^{(l)} \\ &= \left(c\delta t_{uw} + \epsilon_{pr,uw}^{(k)}\right) - \left(c\delta t_{uw} + \epsilon_{pr,uw}^{(l)}\right) \\ &= \epsilon_{pr,uw}^{(k.l)}\end{aligned} \tag{13}$$

For the carrier-phase, this reduction still includes the bias term. However, N is known to have an integer value, and can thus be easily determined and removed to leave only the noise term.

$$\begin{aligned}\rho_{ddcp}^{(k,l)} &= \rho_{ddcp}^{(k)} - \rho_{sdcp}^{(l)} \\ &= \left(c\delta t_{uw} + \lambda N_{uw}^{(k)} + \epsilon_{cp,uw}^{(k)}\right) - \left(c\delta t_{uw} + \lambda N_{uw}^{(l)} + \epsilon_{cp,uw}^{(l)}\right) \\ &= \lambda N_{uw}^{(k,l)} + \epsilon_{cp,uw}^{(k.l)}\end{aligned} \tag{14}$$

These double-differenced signals are formed between all satellites at a given epoch that have the same C/N_0. Once a large number of these samples have been accumulated, the standard deviation can be calculated for the double-differenced measurements, which in turn can be related back to the undifferenced standard deviation by

$$\begin{aligned} \sigma_{pr} &= \frac{\sigma_{ddpr}}{2} \\ \sigma_{cp} &= \frac{\sigma_{ddcp}}{2} \end{aligned} \tag{15}$$

An analytical model for the noise is given by [30]

$$\begin{aligned} \sigma_{pr} &= \frac{c}{1.023 \cdot 10^6} \sqrt{\frac{b_{dll}}{SNR}} \\ \sigma_{cp} &= \frac{\lambda}{2\pi} \sqrt{\frac{b_{pll}}{SNR}} \\ SNR &= 10^{\frac{C/N_0}{10}} \end{aligned} \tag{16}$$

This is a function of the signal-to-noise ratio SNR and the bandwidths of the tracking loops b.

The receiver noise for the pseudorange and carrier-phase measurements as a function of C/N_0 is shown in Figure 10. The trends for both measurements match closely with the analytical solution. The level of pseudorange noise is < 35 cm, with the mean value of 20 cm being approximately double that of the measurement residuals seen during the static receiver testing (cf. Figure 9). This is precisely what is expected when using GRAPHIC measurements in the filter. The carrier-phase noise values of the AsteRx4 receiver are on the order of 1 mm, confirming its suitability for use with precision navigation of small satellites.

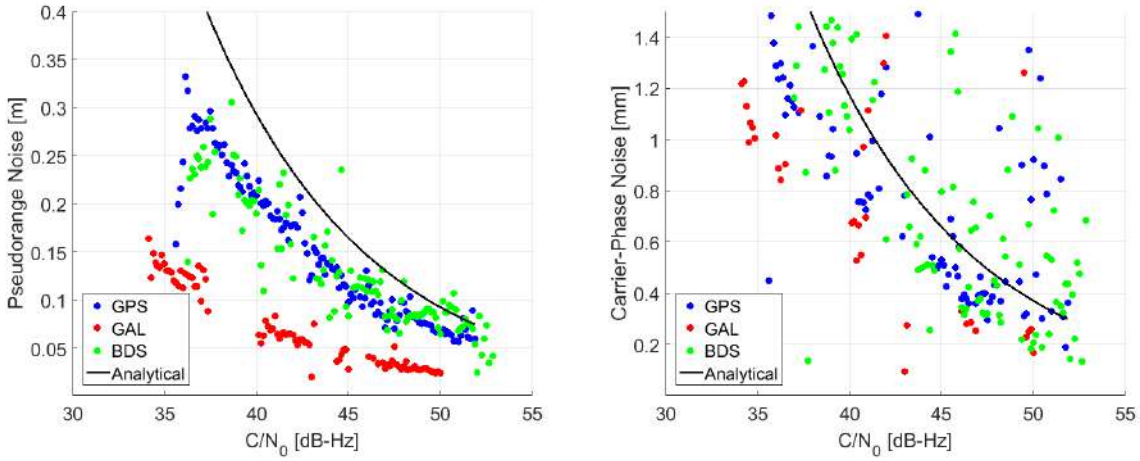

Figure 10: Measurement noise of an AsteRx4 receiver for pseudorange (left) and carrier-phase (right).

4 Satellite Dynamics Simulation Software

The precise simulation of orbital trajectories through numerical integration is a core component of the testbed development. In this section, the details of the orbit modeling software and its validation against PRISMA mission flight products [31] are shown and discussed.

The high-fidelity simulation of large satellite formations in real-time motivated the development of a high-performance software library. The custom-built software library developed to support the testbed is called Space Rendezvous Lab Satellite Software, also known as $\mathcal{S}^3$. This software library is written in C/C++ to limit the computational overhead from the language. An additional benefit of this design choice is that core functionality (like orbit propagation) is widely portable, requiring few changes to implement on flight computers. At the same time, C/C++ is not the most user-friendly language for use in research and development. Therefore, the core functionality is also made accessible in the MATLAB/Simulink environment through the use of MEX function-wrappers and S-Functions. This has the added benefit of allowing a model-based approach to satellite simulation in the real-time dynamics propagation. An overview of the $\mathcal{S}^3$ software modules and functionality is shown in Figure 11.

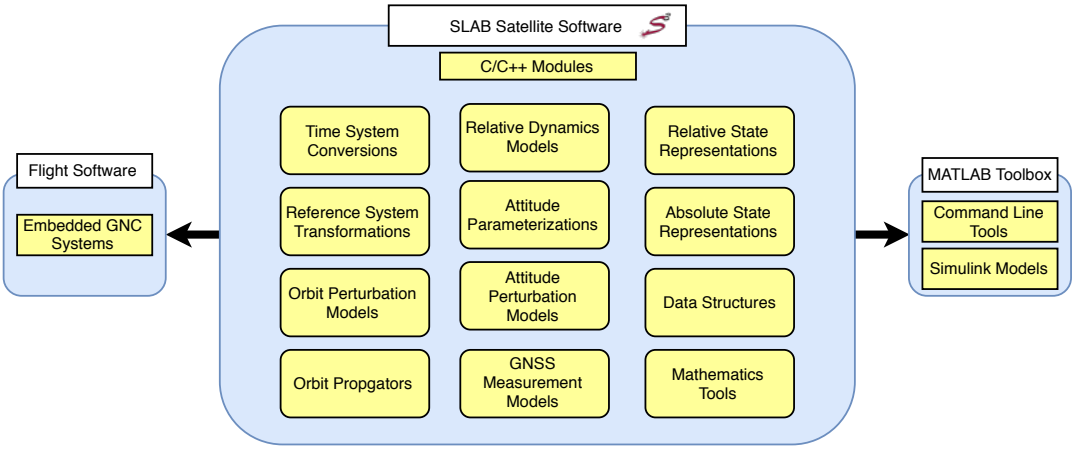

Figure 11: SLAB Satellite Software modules and software structure.

Since one of the desired use-cases of the testbed is to validate novel orbit determination techniques for high-precision applications like gravity recovery, an effort was made to implement the most recent models for all orbit perturbations. Due to the complexity of some models such as solid Earth and ocean tides, not all desired models are currently implemented. All models currently available for use in testbed simulations are listed in Table 4.

To validate the perturbation models, a comparison was performed between the $\mathcal{S}^3$ orbit propagator and PRISMA flight data. The precise orbit determination of the PRISMA mission resulted in absolute orbit positions accurate at the meter level [31, 40]. A set of 96 1-hour sections of PRISMA precise orbit products were compared against 1-hour propagations from $\mathcal{S}^3$, given matching initial conditions. The data was adjusted by removing the 1-hour segments when a maneuver was executed. The days considered were September 20-22, 2010 and March 17, 2011. The results of this comparison are shown in Figure 12. As part of the comparison, two tests were performed to evaluate the effect of perturbation model selection on propagation error. One test used the Harris-Priester density

Orbit Perturbation Model	Description
Gravity Field Model	GGM01S (120x120)[32]
Atmospheric Drag	NRLMSISE-00[33]
	Harris-Priester[34]
	Cannon-ball spacecraft model[34]
Solar Radiation Pressure	Flat plate model[34]
	Conical Earth shadow model[34]
Geomagnetic & Solar Flux Data	NOAA Daily KP AP Indices
Third-Body Perturbations	Analytical Sun & Moon[34]
	DE430 (All planets)[35]
Relativistic Corrections	First-order corrections for special and general relativistic effects[34]
Empirical Accelerations	First-order Gauss-Markov process[36]
Reference Frames	
Reference Frame Conventions	IAU 2010[37, 38]
	EME 2000[34]
Precession/Nutation	IAU 2006/2000A[38]
	IAU 1980/1976[34]
Earth Orientation Parameters	IERS EOP C04 14[39]
	IERS EOP A 08[37]
	IERS EOP B 08[37]
Numerical Integrators	RK4
	Dormand-Prince RK7(8)

Table 4: Orbit perturbation models, corrections, and reference frames supported by $\mathcal{S}^3$ software.

model, while the other test used the more recent NRLMSISE-00 atmospheric density model. All other perturbation models were applied, and were the same between the two tests. The results of the comparison are shown in Table 5. The tests showed that numerical integration of the equations of motion by $\mathcal{S}^3$ is accurate to the level of the PRISMA POD products, with mean propagation error of 1.808 and 1.325 meters after 1 hour, respectively. Furthermore, there is shown to be a small benefit of using the NRLMSISE-00 drag model.

Test Case	Mean Error $[m]$	1σ Error $[m]$
Harris-Priester	1.808	0.587
NRLMSISE-00	1.325	0.540

Table 5: Orbit propagation errors after 1 hour.

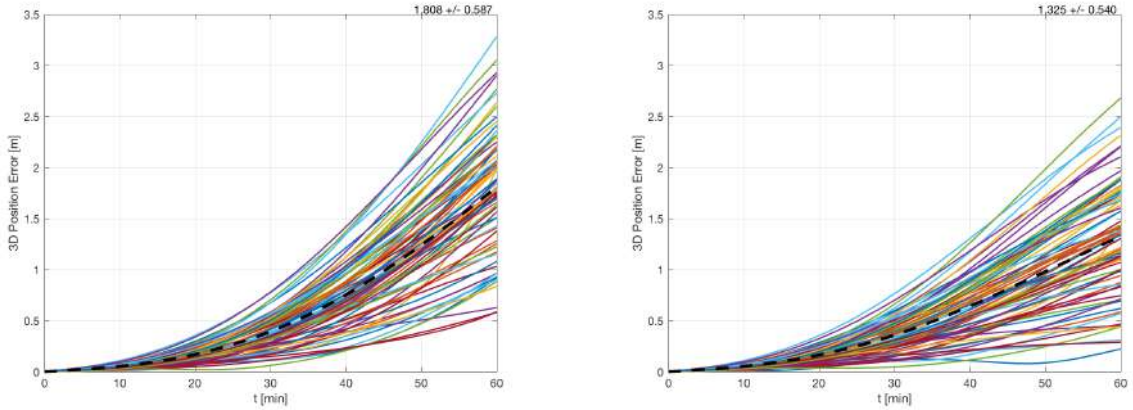

Figure 12: Comparison between full-force model orbit propagation and PRISMA mission flight data using Harris-Priester (left) and NRLMSISE-00 (right). Mean propagation error overlayed in black.

5 HIL Test For DiGiTaL Formation Flying Navigation System

A unique simulation scenario is adopted to demonstrate the application of the SGNT to the validation of the formation-flying navigation algorithms, specifically the prototype algorithms of the DiGiTaL project. Since a core-component of the DiGiTaL algorithms is the ability to scale beyond two spacecraft, a hypothetical formation of four small satellites, configured to perform synthetic aperture radar interferometry, was used. GNSS measurements for this scenario were generated using the IFEN GSS. However, because the scenario involves more than two spacecraft, and the IFEN has only two RF outputs, HIL measurements had to be collected over multiple successive runs using an AsteRx4 receiver. The GNSS-based navigation algorithms were then used to process the simulated data offline in an open-loop test configuration.

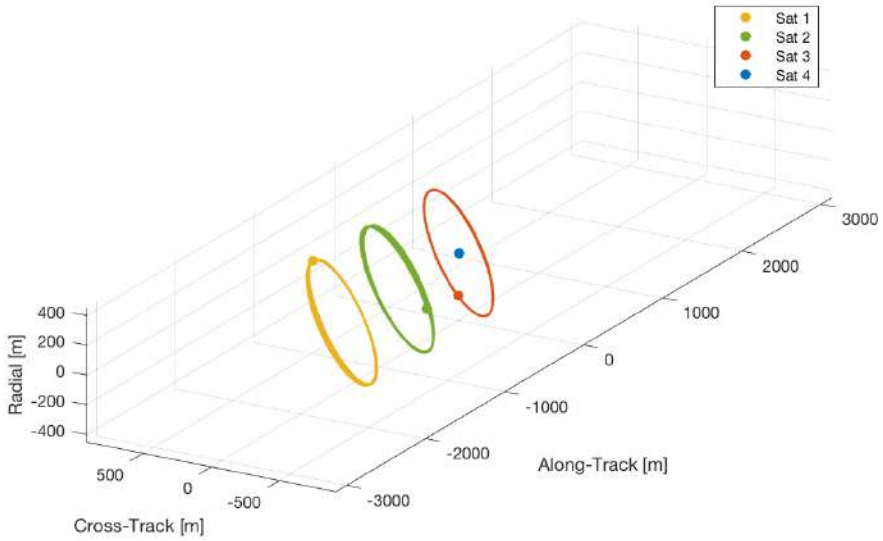

Figure 13: Simulated formation trajectory, as seen in the RTN frame of the satellite 1.

Keplerian Elements	Satellite 1	Satellite 2	Satellite 3	Satellite 4
Semi-major axis (a) [m]	7070863.148	7070861.973	7070865.467	7070868.038
Eccentricity (e) []	6.0e-4	6.0e-4	5.7e-4	6.4e-4
Inclination (i) [°]	98.19	98.19	98.19	98.20
Long. of Ascend. Node (Ω) [°]	0.5879	0.5879	0.5854	0.5855
Arg. of Perigee (ω) [°]	-8.964	-8.965	-11.626	-10.352
Mean Anomaly (M) [°]	227.90	227.89	230.55	229.27

Table 6: Initial orbital elements of the formation.

The navigation filter employs the common extended Kalman filter formulation as described previously, where each satellite in the formation runs its own separate instance of the filter. The filter state is chosen to be the absolute states of the host spacecraft, i, and another pre-set satellite in the formation, j. So long as the pre-set co-estimation states form a strongly connected graph, the precise relative position of any single satellite with respect to any other can, in theory, be reconstructed by sharing state estimate information between satellites. This two-spacecraft state choice

Parameter	Value
Initial Epoch	April 5, 2017, 00:00:00 GPST
Final Epoch	April 5, 2017, 06:00:00 GPST
GNSS Systems	GPS
Constellation Definition	IGS Final Product
Broadcast Ephemeris	RINEX Record
Ionosphere Errors	From RINEX Record
Antenna Gain Pattern	Tallysman TW-3972E

Table 7: Formation flying test configuration.

is made to limit the computational cost of the time and measurement updates compared with a four-spacecraft state. The measurements used by the filter are

$$\mathbf{z} = \left(\boldsymbol{\rho}^{i}_{GR}, \boldsymbol{\rho}^{j}_{GR}, \boldsymbol{\rho}^{ij}_{SDCP} \right) \tag{17}$$

where subscript GR denotes GRAPHIC measurements and subscript $SDCP$ denotes single-difference carrier-phase measurements. The superscript i represents the host spacecraft, and superscript j denotes the second spacecraft. The filter estimation parameters

$$\mathbf{x} = \begin{bmatrix} \mathbf{r}_i & \mathbf{v}_i & \mathbf{a}_i^{emp} & \boldsymbol{c\delta t}_i & \mathbf{N}_i & \mathbf{r}_j & \mathbf{v}_j & \mathbf{a}_j^{emp} & \boldsymbol{c\delta t}_j & \mathbf{N}_j \end{bmatrix}^T \tag{18}$$

comprise the spacecraft position and velocity in the Earth-centered inertial frame $(\mathbf{r}, \mathbf{v})$, three empirical accelerations $\mathbf{a}^{emp}$ in the local orbital frame (aligned along the radial R, along-track T, and cross-track N directions), $\boldsymbol{c\delta t}$ denotes the clock offset from each GNSS constellation time, and $\mathbf{N}$ is the GRAPHIC float bias for each receiver channel. The orbit model for the time update is the GGM01S gravity model including up to degree and order 20. The empirical accelerations, modeled as first-order Gauss-Markov processes, serve to compensate for the reduced-fidelity of the filter dynamics. The state transition and sensitivity matrices are computed through numerical integration of the variational equations where the partial derivatives are approximated using a first-order forward difference.

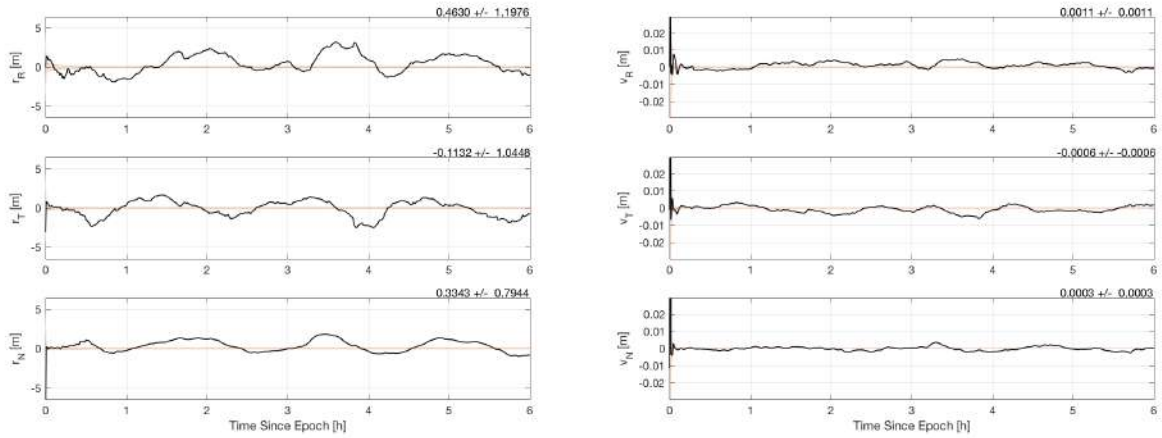

Figure 14: Absolute position (left) and velocity (right) error of satellite 1. Computed by subtracting the simulated truth trajectory from the estimated at each time step.

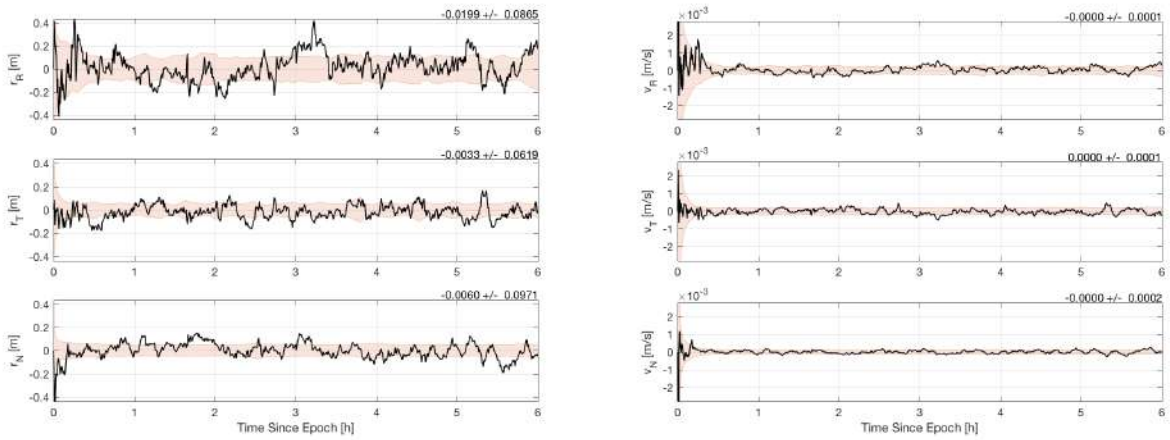

Figure 15: Relative position (left) and velocity (right) error of satellite 2 with respect to satellite 1. Error is mapped into the RTN frame of satellite 1.

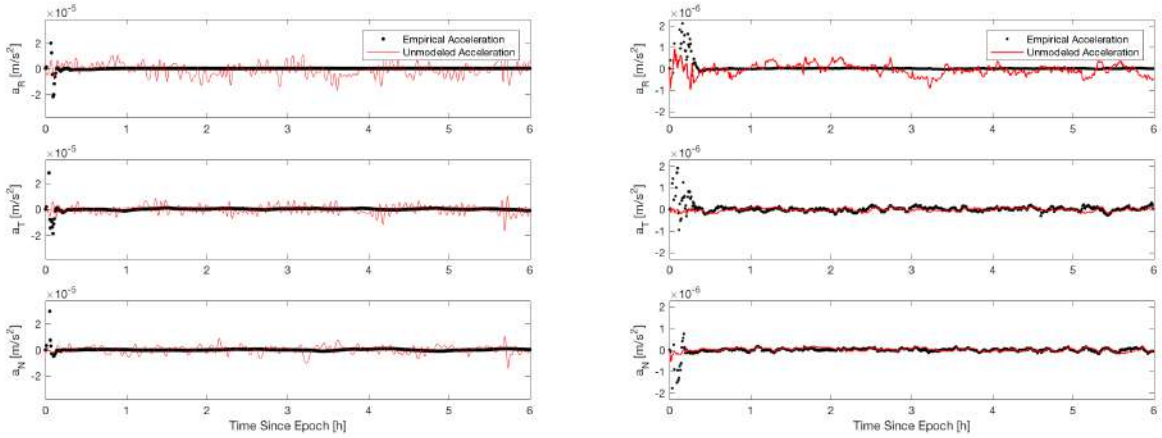

Figure 16: Comparison of empirical acceleration (left) and differential empirical acceleration (right) estimates. The estimated accelerations (black) should track the component of acceleration not modeled by the filter dynamics (red).

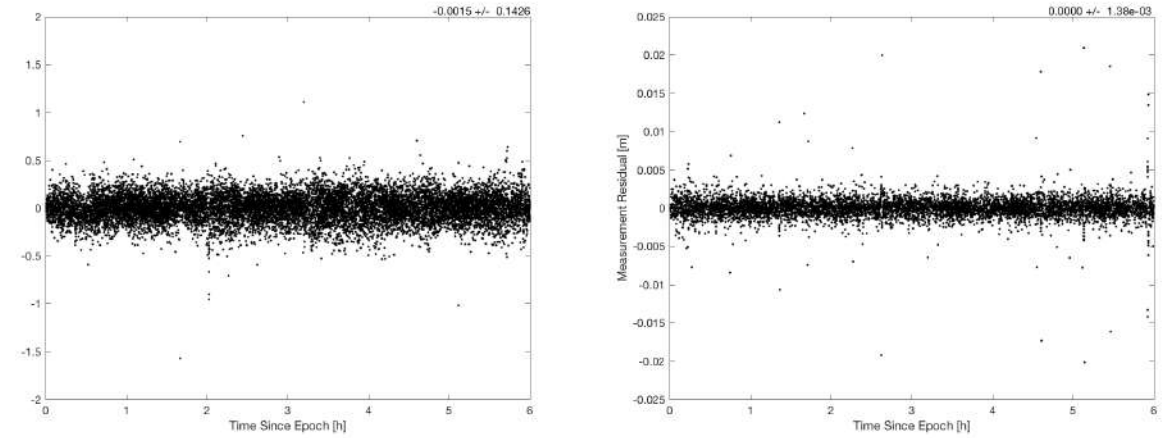

Figure 17: GRAPHIC (left) and single-difference carrier-phase (right) residuals from navigation filter.

Typical results from a 6 hour long simulation are illustrated in Figures 14, 15, 16, and 17. As a matter of conciseness, only the absolute and relative positioning state errors along with estimated empirical accelerations and measurement residuals are shown, as these are the most important indicators of the nominal navigation algorithm performance. In this discussion, the relative position error is always mapped into the orbital frame of satellite i and projected onto the RTN basis. The achieved absolute navigation accuracy is below 1.5 m (1D, rms) and the relative navigation accuracy is below 10 cm (1D, rms). The GRAPHIC and single-difference carrier-phase residuals display banded Gaussian noise with standard deviations of 0.141 m and 1.38 mm, respectively. These noise values are consistent with the levels found during the receiver characterization process (see Figure 10). While the relative state estimate error is both small and properly reflected in the 1σ covariance

bounds, the same can not be said for the absolute state estimate. The absolute state errors display non-trival biases and the 1σ covariance does not properly capture the absolute state error. This effect is currently believed to be a result of improper process noise tuning and lack of measurement data editing. A positive confirmation of the filter performance is that the estimated empirical accelerations broadly track the long-periodic trends of the unmodeled dynamics. Overall, these results are promising indicators that precision navigation of small satellite formations is achievable, but more work must be done to understand the intricacies of parameter tuning and measurement data editing on filter performance.

6 Conclusions and Future Work

This technical note presents the design and development of the Stanford GNSS Navigation Testbed, which enables hardware-in-the-loop simulation of GNC systems for distributed space missions. The design of the testbed was divided into two sections. The first is the environment, where either live or simulated signals are created. This is done through the use of a live roof antenna, a software receiver emulator, or an IFEN GNSS signal simulator. These signals feed into the second section of the testbed, which is the test article. This consists of the GNSS receivers that are used, as well as the GNC algorithms that are being tested. One such focus of the testbed is the Distributed Timing and Localization system, utilizing commercial-off-the-shelf hardware to create an onboard GNSS navigation payload for small satellite formations.

The receiver emulator and IFEN GSS were verified through a static test. The Septentrio roof antenna was used to collect a truth data set. The receiver emulator and GSS were then configured to reproduce the scenario through simulation. A cross-comparison was completed, and consistency was shown in tracking capabilities, signal carrier-to-noise ratios, and achievable navigation solutions. This comparison enabled the use of the GSS for receiver characterization through a zero-baseline test. The measurement noise characteristics of the Septentrio receiver were quantified, and the capability of the testbed to perform this characterization was shown.

To simulate the environmental conditions present in orbital scenarios, the Space Rendezvous Lab Satellite Software ($\mathcal{S}^3$) was developed. This high-performance software package uses the most recent models for orbit perturbations to enable high-fidelity simulation of large satellite formations. Validation was performed against PRISMA flight data, showing accuracy to the level of the PRISMA POD products.

A representative four spacecraft test was conducted using $\mathcal{S}^3$ with the Septentrio AsteRx4 GNSS receiver in the loop. A dual-inertial estimation state was used, comprising of position, velocity, empirical accelerations, clock offsets, and GRAPHIC float biases for two spacecrafts in the formation. The empirical accelerations allow for a reduced dynamic model in the filter time update by estimating the unmodeled effects. Using both GRAPHIC and single-difference carrier-phase measurements, navigation accuracies of 1.5 m and 10 cm were achieved for absolute and relative navigation, respectively.

The test article flight software discussed is still in active development, so a closed-loop HIL test was not possible. In the near future, the flight software development will be completed and embedded into the DiGiTaL system. This will enable closed-loop HIL tests of precision navigation and control systems for small satellites.

Future developmental work includes the integration of integer ambiguity resolution (IAR) techniques to solve for the carrier-phase bias. This allows for the exploitation of the millimeter-level noise of the carrier-phase measurements, leading to centimeter-level positioning precision capabilities. Improvements to the state-of-the-art of IAR includes the investigation of using multi-GNSS, multi-frequency measurements. Other developmental areas include swarm navigation for an arbitrary number of satellites through covariance intersection, and using range-only measurements between spacecraft in GNSS-impaired situations.

References

[1] B. Sullivan, D. Barnhart, L. Hill, P. Oppenheimer, B. L. Benedict, G. Van Ommering, L. Chappell, J. Ratti, and P. Will, "DARPA phoenix payload orbital delivery system (PODs):"FedEx to GEO"," *AIAA SPACE 2013 Conference and Exposition*, San Diego, California, 2013, p. 5484.

[2] J. Kolmas, P. Banazadeh, A. W. Koenig, B. Macintosh, and S. D'Amico, "System design of a miniaturized distributed occulter/telescope for direct imaging of star vicinity," *2016 IEEE Aerospace Conference*, Big Sky, Montana, 2016, pp. 1–11.

[3] O. Montenbruck, G. Allende-Alba, J. Rosello, M. Tossaint, and F. Zangerl, "Precise Orbit and Baseline Determination for the SAOCOM-CS Bistatic Radar Mission," *Proceedings of the 2017 International Technical Meeting of The Institute of Navigation*, Monterey, California, pp. 123–131.

[4] S. D'Amico, J.-S. Ardaens, and R. Larsson, "Spaceborne autonomous formation-flying experiment on the PRISMA mission," *Journal of Guidance, Control, and Dynamics*, Vol. 35, No. 3, 2012, pp. 834–850.

[5] O. Montenbruck, R. Kahle, S. D'Amico, and J.-S. Ardaens, "Navigation and control of the TanDEM-X formation," *The Journal of the Astronautical Sciences*, Vol. 56, No. 3, 2008, pp. 341–357.

[6] S. Bandyopadhyay, G. P. Subramanian, R. Foust, D. Morgan, S.-J. Chung, and F. Hadaegh, "A review of impending small satellite formation flying missions," *53rd AIAA Aerospace Sciences Meeting*, Kissimmee, Florida, 2015, p. 1623.

[7] O. Montenbruck and R. Kroes, "In-flight performance analysis of the CHAMP BlackJack GPS Receiver," *GPS solutions*, Vol. 7, No. 2, 2003, pp. 74–86.

[8] V. Capuano, C. Botteron, and P.-A. Farine, "GNSS Performances for MEO, GEO and HEO," *64th International Astronautical Congress*, Beijing, China, 2013.

[9] J. Leitner, "A hardware-in-the-loop testbed for spacecraft formation flying applications," *Aerospace Conference, 2001, IEEE Proceedings.*, Vol. 2, IEEE, 2001, pp. 2–615.

[10] R. Burns, B. Naasz, D. Gaylor, and J. Higinbotham, "An environment for hardware-in-the-loop formation navigation and control," *AIAA/AAS Astrodynamics Specialist Conference and Exhibit*, Providence, Rhode Island, 2004, p. 4735.

[11] E. Gill, B. Naasz, and T. Ebinuma, "First results from a hardware-in-the-loop demonstration of closed-loop autonomous formation flying," *26th Annual AAS Guidance and Control Conference*, Breckenridge, Colorado, 2003.

[12] L. B. Winternitz, W. A. Bamford, S. R. Price, J. R. Carpenter, A. C. Long, and M. Farahmand, "Global Positioning System Navigation Above 76,000 km for NASA's Magnetospheric Multiscale Mission," *39th AAS Guidance, Navigation and Control Conference*, Breckenridge, Colorado, 2016.

[13] S. Leung and O. Montenbruck, "Real-time navigation of formation-flying spacecraft using global-positioning-system measurements," *Journal of Guidance, Control, and Dynamics*, Vol. 28, No. 2, 2005, pp. 226–235.

[14] S. D'Amico, S. De Florio, J.-S. Ardaens, and T. Yamamoto, "Offline and hardware-in-the-loop validation of the GPS-based real-time navigation system for the PRISMA formation flying mission," *3rd International Symposium on Formation Flying, Missions and Technology*, Noordwijk, Netherlands, 2008, pp. 23–25.

[15] T. Yamamoto and S. D'Amico, "Hardware-in-the-loop demonstration of GPS-based autonomous formation flying," *4th ESA Workshop on Satellite Navigation User Equipment Technologies*, Noordwijk, Netherlands, 2008.

[16] S. A. Kowalchuk, *Investigation of nonlinear control strategies using GPS simulator and spacecraft attitude control simulator.* PhD thesis, Virginia Polytechnic Institute and State University, 2007.

[17] J.-I. Park, H.-E. Park, S.-Y. Park, and K.-H. Choi, "Hardware-in-the-loop simulations of GPS-based navigation and control for satellite formation flying," *Advances in Space Research*, Vol. 46, No. 11, 2010, pp. 1451–1465.

[18] O. Montenbruck, M. Wermuth, A. Hauschild, G. Beyerle, A. Helm, S. Yudanov, A. Garcia, and L. Cacciapuoti, "Multi-GNSS Precise Orbit Determination of the International Space Station (ISS)," *2013 International Technical Meeting of The Institute of Navigation*, 2013, pp. 808–820.

[19] S. Biswas, L. Qiao, and A. Dempster, "Space-borne GNSS based orbit determination using a SPIRENT GNSS simulator," *15th Australian Space Research Conference*, Adelaide, Australia, 2014.

[20] J. M. Dow, R. E. Neilan, and C. Rizos, "The international GNSS service in a changing landscape of global navigation satellite systems," *Journal of Geodesy*, Vol. 83, No. 3, 2009, pp. 191–198.

[21] "IFEN Product Overview," http://www.ifen.com/products/products-overview.html. Accessed: 2016-11-30.

[22] "Spectracom TSync Product Page," https://spectracom.com/products-services/precision-timing/tsync-timecode-processors. Accessed: 2017-04-26.

[23] N. R. Canada, "Online Glocal GPS Processing Service (CSRS-PPP)," 2010. Natural Resources Canada. Online Global GPS Processing Service (CSRS-PPP). *http : //www.geod.nrcan.gc.ca/products − produits/ppp$_e$.php* (2010).

[24] P. Tetrault and P. Sauve, "CSRS-PPP: A web tool to facilitate NAD83(CSRS) integration," tech. rep., Ontario Professional Surveyor, 2010.

[25] T. Yunck, *Coping with the Atmosphere and Ionosphere in Precise Satellite and Ground Positioning in: Environmental Effects on Spacecraft Trajectories and Positioning.* Washington, D.C.: American Geophysical Union, 1993.

[26] MOPS, *Minimum Operational Performance Standards for Global Positioning System/Wide Area Augmentation System Airborne Equipment.* Document No. RTCA/DO-229A, 1998.

[27] A. E. Niell, "Global mapping functions for the atmosphere delay at radio wavelengths," *Journal of Geophysical Research*, Vol. 101, 1996, pp. 3227–3246.

[28] S. D'Amico, *Autonomous Formation Flying in Low Earth Orbit*. PhD thesis, TU Delft, Delft University of Technology, 2010.

[29] O. Montenbruck and C. Renaudie, "Phoenix-S/-XNS performance validation," *DLR/GSOC GTN-TST-0120*, 2007.

[30] P. Ward, *Satellite Signal Acquisition and Tracking, in Understanding GPS, Principle and Applications*. Kaplan.

[31] J.-S. Ardaens, O. Montenbruck, and S. D'Amico, "Functional and performance validation of the PRISMA precise orbit determination facility," *ION International Technical Meeting*, San Diego, California, 2010, pp. 25–27.

[32] B. D. Tapley, S. Bettadpur, M. Watkins, and C. Reigber, "The gravity recovery and climate experiment: Mission overview and early results," *Geophysical Research Letters*, Vol. 31, No. 9, 2004.

[33] J. Picone, A. Hedin, D. P. Drob, and A. Aikin, "NRLMSISE-00 empirical model of the atmosphere: Statistical comparisons and scientific issues," *Journal of Geophysical Research: Space Physics*, Vol. 107, No. A12, 2002.

[34] O. Montenbruck and E. Gill, "Satellite orbits," *Springer*, Vol. 2, 2000, pp. 257–291.

[35] W. M. Folkner, J. G. Williams, D. H. Boggs, R. S. Park, and P. Kuchynka, "The planetary and lunar ephemerides DE430 and DE431," *Interplanet. Netw. Prog. Rep*, Vol. 196, 2014, p. C1.

[36] R. Kroes, *Precise relative positioning of formation flying spacecraft using GPS*. PhD thesis, TU Delft, Delft University of Technology, 2006.

[37] G. Petit and B. Luzum, "IERS conventions (2010)," tech. rep., DTIC Document, 2010.

[38] IAU SOFA Board, "IAU SOFA Software Collection,"

[39] C. Bizouard and D. Gambis, "The combined solution C04 for Earth orientation parameters consistent with international terrestrial reference frame 2005," *Geodetic reference frames*, pp. 265–270, Springer, 2009.

[40] J.-S. Ardaens, S. D'Amico, and O. Montenbruck, "Final commissioning of the PRISMA GPS navigation system," *Journal of Aerospace Engineering*, Vol. 4, No. 3, 2012, p. 105.